Semi-automatic Image Registration of MRI to CT Data of the Prostate Using Gold Markers as Fiducials

Jorn A. van Dalen, H.J. Huisman, A. Welmers, and J.O. Barentsz

University Medical Center St. Radboud, Department of Radiology
Geert Grooteplein-Zuid 10, Postbus 9101, 6500 HB Nijmegen, The Netherlands
J.vanDalen@rad.umcn.nl

Abstract. An accurate image registration of MRI to CT data is of great benefit for prostate treatment planning in image-guided radiotherapy. However, prostate motion with respect to surrounding structures and absence of clear structures in and of the prostate in the CT image, complicate this registration. Therefore, we developed a semi-automatic method for a robust, accurate and time efficient image registration of MRI to CT data of the prostate, making use of gold markers, that are inserted in the prostate, as fiducials. The gold markers, as they appear on both images, are segmented using a thresholding technique. The registration deals with a rigid transformation and is based on the iterative closest point algorithm that acts onto the surfaces of the segmented gold markers. The method is clinically tested and uncertainties of 0.4-0.5 mm and 0.7-1.4 mm are obtained at the centre and at the rim of the prostate, respectively.

1 Introduction

Modern medicine frequently employs several imaging techniques within a single patient's case. These different modalities show different, complementary and (or) partially overlapping aspects of the anatomy examined, or show functional aspects, giving few anatomical pointers. Consequently, several medical specialities might benefit from combining images stemming from two or even more modalities.

In many cases, proper integration of different information facilitates correct clinical diagnosis or treatment, see, e.g., [1, 2] . The determination of the geometrical transformation of one of the acquired images to fit another one, i.e., registration, is the first step in this integration process. The second step of the integration is the fusion, required for the integrated display of the data involved. This mainly concerns an adequate visualization.

Since the use of intensity modulated radiation therapy (IMRT), precise external beam radiotherapy treatments can be given to patients [3,4]. In case of the prostate, functional magnetic resonance imaging (MRI), by means of dynamic contrast enhanced MRI (DCE-MRI), using an endo-rectal coil with balloon, H-MR Spectroscopic Imaging (MRSI) and a combination of these two modalities,

J.C. Gee et al. (Eds.): WBIR 2003, LNCS 2717, pp. 311–320, 2003.

have been shown to give precise tumor localization [5,6,7,8,9,10,11]. Functional MRI can thus be used for treatment planning in image-guided radiotherapy. However, to do so, functional MRI data have to be integrated with computed tomography (CT) data, since CT-density information is used to calculate the dose distribution during the treatment planning.

The accuracy required from the image registration procedure can be derived from a consideration of the role of geometrical uncertainties in all steps of the radiotherapy process [12, 13], e.g., uncertainties due to prostate position variations and due to patient set-up variations. To account for these uncertainties in the radiotherapy process, a margin is chosen around the clinical target volume. The accuracy of the registration should thus be such that no noticeable margin increase is necessary. Investigation of the patient set-up variations [14] and prostate position variations by means of daily portal imaging of implanted fiducial gold markers [15], led to an accuracy requirement for the image registration of about 2 mm [15]. Furthermore, the geometrical accuracy required in treatment planning and dose delivery of IMRT is also typically 2 mm [16]. Therefore, the accuracy of the registration should be well below this value.

Since prostate motion with respect to surrounding structures is present [17, 18, 19], such an accurate registration of MRI to CT data of the prostate, using these surrounding structures, e.g., bony structures, is not available. Therefore, a registration method of MRI to CT data of the prostate is wanted that does *not* make use of surrounding structures. The main difficulty, however, is the absence of clear structures in the CT image of and in the prostate. In [15], a clinically tested three-dimensional image registration of MRI to CT data of the prostate is presented, making use of gold markers, that were inserted in the prostate, as fiducials. Using these markers for the registration of CT and MRI images in the radiation treatment planning of localized prostate cancer, was also suggested by [20]. The registration performed in [15] is based on manually segmented markers giving accurate results, i.e., uncertainties less than about 2 mm, in most cases. However, in some cases big outliers of about 5 to 15 mm are observed. Furthermore, the manual segmentation is time consuming.

Therefore, we developed a *semi-automatic* three-dimensional image registration of MRI to CT data of the prostate, also making use of gold markers, as fiducials. With the limited user interaction we want to improve the accuracy and robustness of the registration and make it more time efficient.

To perform the registration and test its performance, a database of 20 patients is used. A comparison is made to the results of [15].

2 Materials

In this study, similar materials are being used as in the study of [15]. The database consists of images of 20 consecutive patients with histologically confirmed prostate cancer.

Gold markers that were inserted in the prostate serve to measure and to correct the prostate position during all fractions of the radiotherapy treat-

Table 1. Specifications of the CT and the anatomic MRI scans. For all types the pixel size (PS) in the sagittal-coronal plane, slice thickness (ST) in the axial direction, and field of view (FOV) are given. For the CT scan, the X-ray high voltage peak (V) and the dose rate (R) are given; For the MRI scans the repetition time (TR), echo time (TE) and flip angle (FA) are given. When there is no unique value, a range is given.

modality	PS (mm^2)	ST (mm)	FOV (mm)	V (kVp)	R (mAs)
CT	0.69-0.95	3	354-486	130-140	150-170

modality	PS (mm^2)	ST (mm)	FOV (mm)	TR (ms)	TE (ms)	FA (deg)
MRI T2	0.55	5	280	3500-4400	132	180
MRI T2*	0.56-0.78	3	200-285	699-1100	18-25.8	30

ment [19, 21]. Gold markers were chosen, since they can be visualized in the portal images made during radiotherapy treatment using the transmitted high-energy photon beam of the linear accelerator. About two weeks before performing the imaging studies, on average four gold markers, but not more than five or less than three, with a length of 5 or 10 mm and a thickness of 1 mm, were inserted through trans-rectal ultrasound guidance by an urologist. Usually, two gold markers were inserted at the base, one at the apex and one at the centre of the prostate. In this study, the markers were used as fiducials for the image registration.

The imaging protocol consisted of two examinations. Firstly, CT was performed using a multi-slice spiral CT scanner (Marconi AcQsim, Cleveland, USA) with specifications as given in Table 1. In twelve patients an endo-rectal coil with balloon, with a similar design as the commercially available MRI endo-rectal coil (Medrad, Pittsburgh, US), was inserted and inflated with 80 cc of air, before the CT scan was taken.

Secondly, MRI was conducted using a 1.5 T scanner (Siemens Sonata, Erlangen, Germany). T2-weighted turbo spin echo (TSE) sequences in three planes were acquired. A T2*-weighted sequence (a multi-echo data image combination (MEDIC)) was acquired at the same slice location as the axial T2-weighted TSE sequence. Specifications of the these anatomical MRI scans can be found in Table 1. Apart from the anatomical MRI scans, functional MRI scans were taken. Magnetic resonance spectroscopic imaging was performed using the 3D-PRESS sequence. A multi-slice T1-weighted gadolinium-enhanced FLASH sequence was also performed. For all patients the endo-rectal coil with balloon was inserted before the MRI scans were taken. Using this endo-rectal coil, the MRI image quality improved due to a significant increase of the signal-to-noise ratio. The total examination time took about 60 minutes. Since no significant motion artefacts were observed in this time, it is assumed that accurate matches can be obtained between the functional and anatomic MRI images.

Imaging data were transferred to a PC for post-processing. Using image viewing and registration software, based on Tcl/Tk [22] and the visualization toolkit VTK [23], the gold markers, as they appear on the CT scan as hyper dense and on the T2*-weighted MRI images as low signal intensity areas, were used for

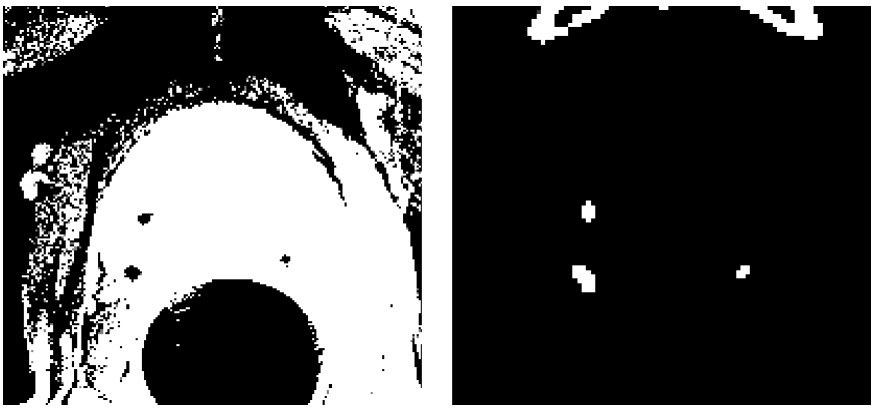

Fig. 1. An MRI and a CT slice of the prostate after thresholding, where three markers are clearly visible.

semi-automatic segmentation and subsequently registration. Due to the length of the markers, their orientation and the slice thickness of both images, the markers are visible in at least one slice, but in most cases in two or three slices.

3 Methods

To achieve a successful registration, first a segmentation of the prostate markers is performed. The semi-automatic segmented markers are used for the registration, where the ICP algorithm is applied onto the surfaces of those segmented markers. The registration is based on a rigid transformation, i.e., based on three translation and three rotation parameters.

3.1 Segmentation

Firstly, the user indicates the centre of the markers, denoted by seeds, $\boldsymbol{s}_m$, where m represents the seed number, as good as possible, on both the MRI and CT images. Since the gold markers are easy to find on the CT image, but less easy on the MRI image, the user can manually align the MRI and the CT image. This will assist him to identify the markers on the MRI image. Both on the MRI as on the CT image, an equal number of seeds is indicated.

Secondly, a binary thresholding is performed on both images. The markers can then be identified by isolated clusters of voxels, with dimensions of about $1.0 \times 0.3 \times 0.3$ cm and with grey values below a threshold T_{MRI} for the MRI image and above a threshold T_{CT} for the CT image. Figure 1 shows an example of an MRI and a CT slice after thresholding, where three markers are clearly visible.

Next, only information is considered within those ellipsoids with centres given by $\boldsymbol{s}_m$ and radii of 1.5 cm in the axial (z) direction and 0.5 cm in both the sagittal

(x) and coronal (y) direction. The set of volumes given by the voxels within the ellipsoids is denoted by V. This mask avoids voxels that are relatively far from the markers, but having about the same grey value as those that compose the marker, to be used in the segmentation.

To obtain the segmented markers, the voxels within the same grey value range (below T_{MRI} for the MRI and above T_{CT} for the CT image) and those that are connected (via neighbouring voxels within the same grey value range) to the user supplied seeds, $\boldsymbol{s}_m$, are marked. Clusters, C_m, of these marked voxels, $v_{m,n}$ (with n the voxel number), then represent the markers, i.e.,

$$C_m = \{v_{m,n} | v_{m,n} \in V\} \quad . \tag{1}$$

Next, triangulated iso surfaces are determined using the boundary value of the clusters as the contour value. Finally, normals are computed for these surfaces, for each of the polygonal facets. The normals are computed via the cross product $[v_1 - v_2] \times [v_2 - v_3]$, where v_1, v_2 and v_3 are three vertices of the polygon, and are averaged at shared points. Using these normals, a faceted shading of the surface is obtained, that will be used as an input of the ICP algorithm. The iso surfaces and the normals are computed using the VTK methods vtkContourFilter and vtkPolyDataNormals [23], respectively.

3.2 Registration

To achieve a successful registration, it is important that first an initial estimate of the relative pose of the two prostate images is given. This is done by roughly aligning the two images, in the region of the prostate, manually. Then, the ICP algorithm performs the final registration step, automatically.

The iterative closest point algorithm [24,25,26] is a method for the registration of three-dimensional shapes. It works in terms of registration of collected data, which are converted to a point set $P = \{\boldsymbol{p}_i\}$, of image 1, to model shape data X, which remain in their original representation, of image 2. In this paper, P is a point set located onto the surface of the segmented MRI markers and X is the surface of the segmented CT markers.

The algorithm has three stages and iterates. The first step is finding the closest model point $\boldsymbol{x}_i \in X$ with respect to $\boldsymbol{p}_i$ for all i. The point $\boldsymbol{x}_i \in X$ for which the distance $d(\boldsymbol{p}_i, X)$ between $\boldsymbol{p}_i$ and $\boldsymbol{x}_i$ is minimum, can be derived from

$$d(\boldsymbol{p}_i, X) = \min_{\boldsymbol{x}_i \in X} |\boldsymbol{x}_i - \boldsymbol{p}_i| \quad . \tag{2}$$

For a triangulated surface - the model representation of the image data that is being used - the model X comprises a set of triangles $T = \{t_k\}$. If triangle t_k has vertices $\boldsymbol{r}_{k,j}$ $(j = 1, 2, 3)$, then the minimum distance between $\boldsymbol{p}_i$ and t_k is

$$d(\boldsymbol{p}_i, t_k) = \min_{u+v+w=1} |u\boldsymbol{r}_{k,1} + v\boldsymbol{r}_{k,2} + w\boldsymbol{r}_{k,3} - \boldsymbol{p}_i| \quad , \tag{3}$$

where u, v and w are in $[0, 1]$. Thus, the closest distance between the point $\boldsymbol{p}_i$ and the triangle set T is given by

$$d(\boldsymbol{p}_i, T) = \min_k d(\boldsymbol{p}_i, t_k) \quad . \tag{4}$$

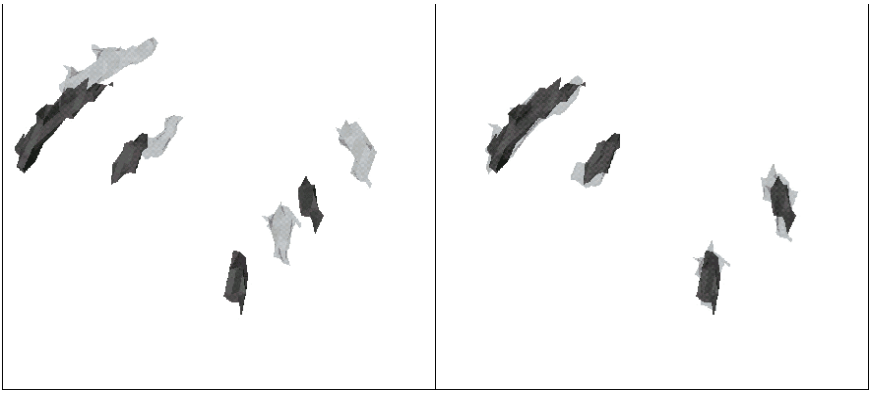

Fig. 2. Four segmented markers in both MRI (dark) and CT (light) images, in 3D, before (left) and after (right) applying the ICP method.

The closest model point to the data point $\boldsymbol{p}_i$ is then given by $\boldsymbol{x}_i = (u\boldsymbol{r}_{k,1}, v\boldsymbol{r}_{k,2}, w\boldsymbol{r}_{k,3})$, where $\boldsymbol{r}_{k,j}$ are the vertices of t_k that satisfies Equation (4).

Secondly, a least square registration between the points $\{\boldsymbol{p}_i\}$ and $\{\boldsymbol{x}_i\}$ can be carried out by minimizing

$$f(\boldsymbol{q}) = \frac{1}{N_\mathrm{p}} \sum_{i=1}^{N_\mathrm{p}} |\boldsymbol{x}_i - R(\boldsymbol{q}_\mathrm{R})\boldsymbol{p}_i - \boldsymbol{q}_\mathrm{T}|^2 \quad . \tag{5}$$

where N_p is the number of point pairs being used, $R(\boldsymbol{q}_\mathrm{R})$ is a rotation matrix and $\boldsymbol{q} = (\boldsymbol{q}_\mathrm{R}, \boldsymbol{q}_\mathrm{T})$, resulting from $\arg\min_{\boldsymbol{q}} f(\boldsymbol{q})$, is the transformation vector consisting of three rotation parameters $\boldsymbol{q}_\mathrm{R} = (\alpha_1, \alpha_2, \alpha_3)$ and three translation parameters $\boldsymbol{q}_\mathrm{T} = (T_x, T_y, T_z)$. The function $f(\boldsymbol{q})$ is a measure of the accuracy of the method: the value of $\sqrt{f(\boldsymbol{q})}$ could be interpreted as a standard deviation, giving a measure of the uncertainty of the matching.

Thirdly, the set of data points $\{\boldsymbol{p}_i\}$ is then transformed to $\{\boldsymbol{p}_i'\}$ using the calculated rigid body transformation. Then, the iteration procedure starts by redetermining the closest point set using $\{\boldsymbol{p}_i'\}$ and X. The algorithm terminates when the change in $f(\boldsymbol{q})$ between two successive iterations falls below a threshold. In this analysis this change is set to 0.0001 mm. It also terminates when the number of iterations exceeds 3000. Furthermore, N_p is set to 5000.

An example of the performance of the ICP method is shown in Figure 2: four segmented markers in both MRI and CT images, in 3D, before and after applying the ICP method are visualized. Typically, the ICP registration takes a few seconds.

3.3 Evaluation

For each patient, the computed ICP registration transformation, M, consisting of three rotation and three translation parameters, is applied onto two points

in the MRI image. The first point, $\tilde{\boldsymbol{c}}$, is the average value of the centre-of-mass points of the segmented MRI markers. This point, which is determined by one user, estimates the centre of the prostate. The second point, $\tilde{\boldsymbol{r}}$, is defined as being 2 cm back and down and to the left, with respect to $\tilde{\boldsymbol{c}}$, which would be in the rectum wall region. The resulting points $\boldsymbol{c} = (c_x, c_y, c_z) = M\tilde{\boldsymbol{c}}$ and $\boldsymbol{r} = (r_x, r_y, r_z) = M\tilde{\boldsymbol{r}}$ are thus estimations of the centre and the rim of the prostate after applying the ICP registration.

Inter- and intra-operator variability of the parameter values c_i and r_i ($i = x, y, z$) were determined, in order to get a measure of the registration uncertainty around the centre and the rim of the prostate. This measure assumes that a rigid transformation is sufficient to register the segmented MRI markers onto the segmented CT markers. Variability can be expected on the basis of the user input: how many and which markers does the user select and what threshold values does he use for the segmentation. One operator performed the segmentation and registration five times for five data sets in order to obtain the intra-operator variability. Variability in the registration between three different operators (the inter-operator variability) was measured via a multivariate analysis of variance (MANOVA) test [29]. Furthermore, the effect of using an endo-rectal balloon in the CT images was investigated. All variabilities are obtained via R [30], a freely available language and environment for statistical computing and graphics.

4 Results

The threshold values that are used in the segmentation are set to $T_{\mathrm{MRI}} = 150$ and $T_{\mathrm{CT}} = 900$, with a possible change by the user of ± 50 and ± 400, respectively. Experimentally, these are found to be good values to isolate the gold markers and thus to perform a marker segmentation in both the MRI and CT images.

Studying the variability of the registration results, the MANOVA test suggests that contributions to the variability of intra-operator and balloon effects are not statistically significant. There is a slight effect ($p < 0.08$) due to repeated registrations by different operators. The contribution of inter-operator variability, however, is small.

Figure 3 shows box plots of the total variability of the coordinates c_i and r_i ($i = x, y, z$) after normalization with respect to the mean, per patient.

The three patients in which the biggest variations are observed are patients 3, 5 and 14. The variations are caused by having missed one marker by one user on the MRI image (patients 3 and 14) and by difficulties in getting a good segmentation of hardly visible MRI markers (patient 5).

The estimated total standard deviations at the centre and at the rim of the prostate are given in Table 2. The uncertainties of [15] are also shown.

Our results indicate that the uncertainties are well below the required limit of 2 mm. Furthermore, they are slightly better than the results, excluding the outliers, of [15]. When the outliers observed in [15] are not excluded, our results are much more accurate.

The limited user interaction in our method prevents big outliers to occur and thus makes the method robust and accurate. Moreover, it results in a time effi-

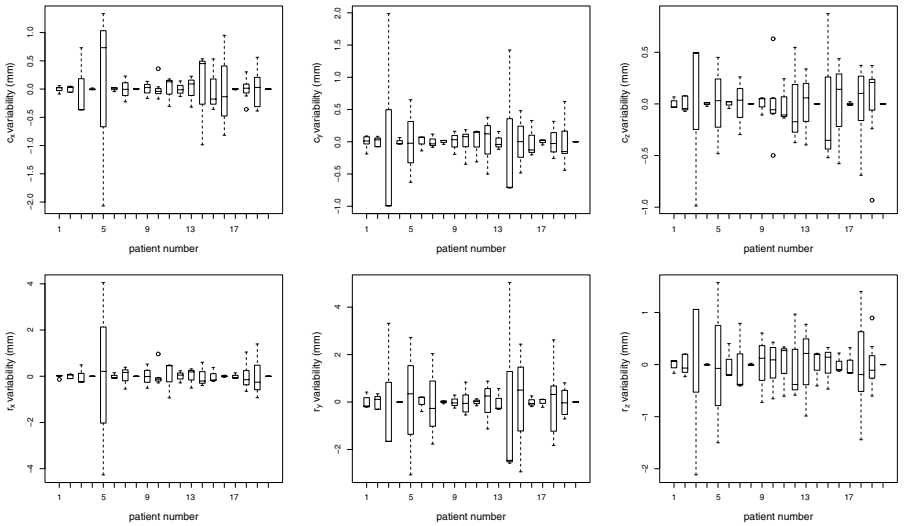

Fig. 3. Box plots of the variability of the coordinates c_i and r_i $(i = x, y, z)$ after normalization with respect to the mean, per patient.

Table 2. Uncertainties, in mm, at the centre, (c_x, c_y, c_z), and at the rim, (r_x, r_y, r_z), of the prostate. Our results and those of [15] are given.

reference	c_x	c_y	c_z	r_x	r_y	r_z
our results	0.5	0.5	0.4	0.9	1.4	0.7
[15] without outliers	0.4	0.6	0.5	1.3	1.5	0.8
[15] with outliers	1.5	2.9	0.9	1.7	3.0	1.1

cient registration: on average, the registration time, from the moment of loading the images till the moment of saving the registration, took about 8 minutes, a factor three less than the time given in [15]. Most likely, the gain in time is due the automation of the segmentation.

5 Conclusions and Discussions

In this paper a semi-automatic method for image registration of MRI to CT data of the prostate is presented, making use of gold markers, that are inserted in the prostate, as fiducials.

The method is clinically tested and uncertainties of 0.4-0.5 mm and 0.7-1.4 mm are obtained at the centre and at the rim of the prostate, respectively. These results are well within the clinical required accuracy for treatment planning in image-guided radiotherapy.

The limited user interaction results in a time efficient registration and prevents big outliers to occur and therefore makes the method robust and accurate. In particular, this is true when comparing to [15], where a similar analysis is

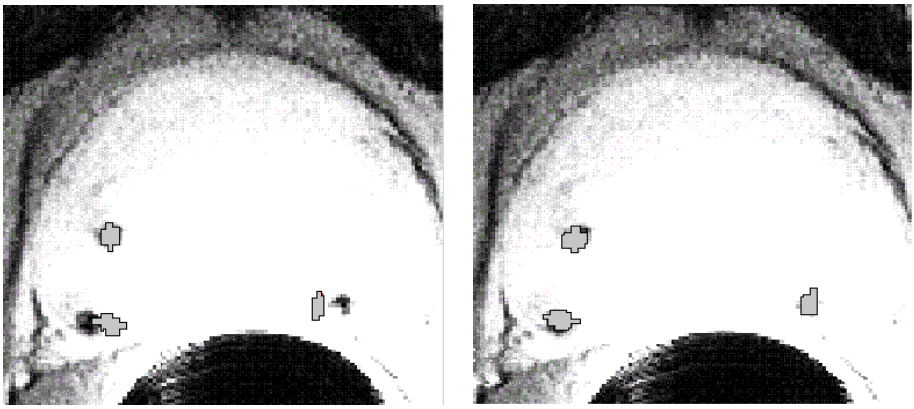

Fig. 4. An extreme example of an MRI and a CT slice of the prostate after ICP registration, where a rigid transformation clearly does not suffice (left), but where an affine transformation gives a much better result (right). The window level of the CT image is such that only the gold markers (indicated by three grey bounded areas) are visible.

performed, but, where the segmentation of the gold markers is performed manually.

In this paper, the assumption is made that a rigid transformation can register the segmented MRI markers onto the segmented CT markers. Thus, it is assumed that imaging artefacts, differences in deformations of the prostate and changes in distance between the markers on CT and MRI images due to marker migration, are negligible and consequently do not affect the registration. This is a strong assumption and found not to be valid for at least some of the patient's images. This is illustrated by the extreme example of Figure 4 where an MRI and CT slice of an image volume of the prostate are shown after applying the ICP registration based on a rigid transformation. A rigid transformation clearly does not suffice here. In 4 (out of 20) patients, we visually observe that a rigid transformation is not able to match the MRI and CT markers. Using an affine transformation, however, where we add three scaling parameters in the transformation, i.e., where we replace $\boldsymbol{q}_{\mathrm{R}}$ of Equation (5) by a vector consisting of 6 elements (three for rotation and three for scaling), we visually observe a much better result. This is also shown in Figure 4.

It has to be investigated further what the registration uncertainties are, quantitatively, as a consequence of assuming that a rigid transformation can register the segmented MRI markers onto the segmented CT markers. Next, it needs to be investigated how non-rigid transformations can improve the registration.

References

1. J.B.A. Maintz and M.A. Viergever, Medical Image Analysis **2** nr. 1 (1998), 1.
2. D.L.G. Hill et al., Phys. Med. Biol. **46** (2001), 1.

3. C. Burman et al., Int. J. Radiat. Oncol. Biol. Phys. **39** nr. 4 (1997), 863.
4. M.J. Zelefsky et al., Radiother. Oncol. **55** nr. 3 (2000), 241.
5. M. Engelbrecht et al., *Dynamic MR imaging of prostate cancer: dynamic features for cancer detection* (2002), submitted to Radiology.
6. M. van der Graaf et al., MAGMA **10** nr. 1 (2000), 153.
7. Y. Kaji et al., Radiology **206** nr. 3 (1998), 785.
8. J. Scheidler, Radiology **213** nr. 2 (1999), 473.
9. J. Kurhanewicz, Radiol. Clin. North. Am. **38** nr. 1 (2000), 115.
10. U. Mueller-Lisse et al., Radiology **221** nr. 2 (2001), 380.
11. F. van Dorsten et al., Radiology **221** nr. P (2001), 585.
12. J. C. Stroom et al., Int J. Radiat. Oncol. Biol. Phys. **43** nr. 4 (1999), 905.
13. M. van Herk et al., Int J. Radiat. Oncol. Biol. Phys. **52** nr. 5 (2002), 1407.
14. E.N. van Lin et al., Int. J. Radiat. Oncol. Biol. Phys. **50** nr. 2 (2001), 569.
15. A. Welmers et al., *3D Image Fusion of CT with Dynamic Contrast Enhanced MRI and MR Spectroscopy of the Prostate Using Gold Markers as Fiducials*, Radiological Society of North America (RSNA) Abstracts, Suppl. to Radiology **225** nr. P (2002), 350. Presented at RSNA 2002.
16. M. Partridge et al., Phys. Med. Biol. **45** nr. 12 (2000), N183.
17. M. van Herk et al., Int. J. Radiat. Oncol. Biol. Phys. **33** nr. 5 (1995), 1311.
18. M.J. Zelefsky et al., Radiother. Oncol. **50** nr. 2 (1999), 225.
19. H. Alasti et al., Int. J. Radiat. Oncol. Biol. Phys. **49** nr. 3 (2001), 869.
20. C.C. Parker et al., Radiother. Oncol. **66** nr. 2 (2003), 217.
21. J.M. Balter, Int. J. Radiot. Oncol. Biol. Phys. **31** nr. 1 (1995), 113.
22. `http://www.tcl.tk/`
23. The Visualization Toolkit User's Guide, ISBN 1-930934-08-4, published by Kitware; The Visualization Toolkit, An Object-Oriented Approach To 3D Graphics, 3rd edition, ISBN 1-930934-07-6, published by Kitware; `http://public.kitware.com/VTK/`
24. P.J. Besl and N.D. McKay, IEEE Transactions on Pattern Analysis and Machine Intelligence **14** nr. 2 (1992), 239.
25. C. Chen and G. Medioni, Image Vision Computing **10** nr. 3 (1992), 145.
26. Z. Zhang, International Journal of Computer Vision **13** nr. 2 (1994), 119.
27. D. Litzenberg et al., Int J. Radiat. Oncol. Biol. Phys. **52** nr. 3 (2002), 699.
28. H. Alasti et al., Int J. Radiat. Oncol. Biol. Phys. **49** nr. 3 (2001), 869.
29. see, e.g., D.F. Morrison, *Multivariate Statistical Methods*, McGraw-Hill (1967), New York; `http://online.sfsu.edu/~efc/classes/biol710/manova/manovanew.htm`
30. `http://www.R-project.org/`